

# MICROSTRUCTURE, MECHANICAL AND CORROSION PROPERTIES OF AISI 904 L SUPER AUSTENITIC STAINLESS STEEL WELDS BY PULSED GAS METAL ARC WELDING PROCESS

P. MANAVALAN & DR. S. RAVI

Department of Manufacturing Engineering, Annamalai University, Annamalai Nagar, Tamil Nadu, India

## ABSTRACT

*This paper deals with the pulsed gas metal arc welding (P-GMAW) of AISI 904 L super austenitic stainless steel when 1.2 mm diameter of Super austenitic stainless steel filler wire was used. 5 mm thick AISI 904 L super austenitic stainless steel sheets were butt welded by pulsed GMAW process with argon as shielding gas. AISI 904 L Super Austenitic Stainless Steel (SASS) has higher levels of Mo, Cr, Ni, N, and Mn under normal conditions. In heating applications, it offers a superior corrosion resistance at moderate and higher temperatures. The microstructure of SASS is exhaustively austenitic in nature, when subjected to a solution-quenched state. The weld quality depends on bead geometry and its microstructure that influence the mechanical properties of the weld. The coarse grained weld microstructure, higher heat-affected zone, and lower penetration together with higher reinforcement reduce the weld service life in continuous mode gas metal arc welding (GMAW) process. Pulsed GMAW is an alternative method providing a better way for overcoming these afore said problems. It uses a higher peak current to allow one molten droplet per pulse, and a lower background current to maintain the arc stability. Current pulsing refines the grains in weld fusion zone with increasing depth of penetration due to arc oscillations. The main aim of the work is to study the effect of various P-GMAW process parameters and their effects with respect to mechanical properties and metallurgical characteristics of the joints. The microstructural characterization of the joints was performed by optical microscopy. The impact and tensile tests were performed and the fracture surface morphology was analysed through scanning electron microscope (SEM). The hardness test was performed along the longitudinal direction of the weld zone with an equal interval of 2 mm. P-GMAW joints were tested for corrosion resistance using potentio dynamic polarization test. The results showed that the joint by P-GMAW process had higher tensile and impact strength than the base metal. The fractography observation showed the cup and cone shaped fracture, while the weld joint showed a mixed mode of fracture. Therefore, the P-GMAW welding is suitable for welding of AISI 904 L super austenitic stainless steel, owing to their excellent mechanical and corrosion properties.*

**KEYWORDS:** P-GMAW, Super Austenitic Stainless Steel, Microstructure Characteristics, Tensile, Impact, Hardness & Corrosion Properties

**Received:** Mar 24, 2019; **Accepted:** Apr 14, 2019; **Published:** May 13, 2019; **Paper Id.:** IJMPERDJUN201987

## INTRODUCTION

Super austenitic stainless steel (SASS) is Fe-based system highly alloyed with Cr, Ni, Mo, and N to produce excellent pitting and crevice corrosion-resistant properties at high temperatures and in seawater. When exposed to elevated temperatures for long periods of time, large amounts of precipitates including carbides, nitrides, and intermetallic phases are formed in this steel. The most commonly observed secondary phases include  $M_{23}C_6$  carbide, and intermetallic  $\sigma$ ,  $\chi$  and Laves phases. Other less commonly observed secondary phases include

$M_6C$ ,  $\pi$ ,  $R$ , and  $Cr_2N$ . High amount of these phases reduces the corrosion resistance and mechanical properties of the stainless steel. The type of precipitate strongly depends on the local composition, heating time and temperature. At temperatures ranging from 700 to 1100°C, carbides are usually the first to form. At longer duration, these carbides are usually replaced by intermetallic compounds such as  $\sigma$ ,  $\chi$  and Laves. Low carbon solubility has been found in  $\sigma$ , while a high solubility of interstitial elements in the austenite ( $\gamma$ ) matrix tends to favour the formation of  $\chi$  and Laves phases. Increased Mo percentage favours the precipitation of intermetallic at higher temperatures. High amount of N (0.5 wt. %) has been found to prevent the  $\chi$  phase from forming at all; instead, the formation of the Laves phase is reported. However, the Laves-phase formation is delayed with additional nitrogen [1-5]. Thus, the addition of nitrogen not only increases the mechanical properties of these materials, but also proves useful in delaying or even preventing the formation of harmful precipitates. Super austenitic stainless steel arouses a good deal of attention as they bridge the gap between relatively cheaper austenitic stainless steel and expensive Nickel base super alloys, when high corrosion properties are required at moderately higher temperatures [6]. The effect of nitrogen increment on the microstructure and mechanical properties of two different austenitic stainless steel welds like 317 L and 904 L austenitic stainless steels finds a place in this study. In 904 L weld, nitrogen had an effect only on its composition and it did not exert any influence on solidification mode, while in 317 L welds, it affects both the solidification mode and composition of the weld [7]. Different super austenitic stainless steels (AISI 904 L, 254 SMO, and AMANOX1.3964) were welded by plasma arc welding and electron beam-welding processes and the resulting microstructural and fatigue properties were studied. In spite of the interdendritic material being saturated with ferrite stabilizing elements (Cr, Mo) the microstructures were completely dendritic and austenitic[8]. In the welding of super austenitic stainless steel Avesta 654 SMO, two different types of precipitates ( $\sigma$  and  $R$ ) were observed in the HAZ. The absence of precipitates in the region near the plate surface, closest to the fusion line, was justified by the cooling rate which was fast enough to prevent the precipitate formation. However, closer to the plate centres, the welding process gave rise to a temperature exposure at which precipitation occurred [9].

The effect of shielding gases on the microstructure and mechanical properties of hybrid laser welded SASS was studied. The authors reported that the shielding gas mixture of 50% He + 45% Ar + 5% O<sub>2</sub> improved the tensile strength [10]. It was reported by Hertzman et al. that autogenous gas tungsten arc welding (GTAW) of super austenitic steel with shielding gases and arc lengths yielding nitrogen content in excess of 0.2% resulted in porosity [11]. The joining of 5-mm-thick plates of super austenitic stainless steel AISI 904L by continuous current (CC) and pulsed current (PC) gas tungsten arc welding (GTAW) using ER2553 and ERNiCrMo-4 fillers was studied. It was found that interface microstructure revealed the absence of deleterious secondary phases at the heat affected zone in all the cases. The average hardness at the fusion zone was found to be higher for PCGTA weldments using ER2553, due to the higher proportions of ferrite [12].

A comparison of metallurgical and mechanical properties of autogeneous and activated compound flux assisted gas tungsten arc welding (GTAW) of AISI 904 L super-austenitic stainless steel was made. The authors found that the compound flux containing 85%SiO<sub>2</sub>–15%TiO<sub>2</sub> accounted for better depth of penetration compared to auto generous welding. And also, it would be highly beneficial to the industries employing super-austenitic stainless steel [13]. Investigations were carried out on the microstructure and mechanical properties of super austenitic stainless steel butt joints by gas metal arc welding with different shielding gas mixtures. Welding was performed under two sets of optimized parameters employing three different shielding gases namely 100% argon, 80% argon+20% CO<sub>2</sub> and 100% CO<sub>2</sub>. They concluded that welds made under 80% argon+20%CO<sub>2</sub> gas under the second set of parameter was found to exhibit comparatively better mechanical properties due to proper amount of the dendritic and interdendritic grain structures in the

weld region [14]. Medium carbon steel (AISI 1030) plates of 10 mm thickness were welded by using the synergic controlled pulsed (GMAW-P) and manual gas metal arc (GMAW) welding techniques. The GMAW-P joints of AISI 1030 steel couples showed superior tensile strength, less grain growth and narrower heat affected zone (HAZ) when compared with GMAW joints and this was mainly due to lower heat input, fine fusion zone grain and higher fusion hardness [15].

As evident from the existing literature, there is a huge demand for AISI 904L super austenitic stainless steel in versatile engineering applications. Hitherto, limited studies had been reported on the weldability of AISI 904L SASS using conventional arc welding process. Since P-GMAW welding process is more advantageous economical and efficient in most of the situations, this work becomes more essential and significant for industries. This study is focused on the weldability of AISI 904L SASS by the P GMAW process using 1.2 mm diameter of super austenitic stainless steel filler wire. The microstructure characterization of these weldments was studied by optical microscopy (OM). The mechanical properties namely tensile strength, impact toughness and microhardness across the welds were studied. The corrosion resistance of the welds were evaluated through the potentiostatic polarization technique. The fractured surface of tensile and impact were analysed through scanning electron microscopy (SEM).

## EXPERIMENTAL PROCEDURE

### Base Material and Welding Procedure

The chemical composition analysis was carried out on the as-received base metal AISI 904L and the filler wire using dry spectroscopic method. The nominal chemical composition of the base and filler metal is given in Table 1.

**Table 1: Base Material Chemical Composition (weight in %)**

Material	Si	Mn	P	S	Cr	Ni	Mo	C	Cu	Nb	V	N	Fe
904L	0.409	1.402	0.035	0.021	20.850	23.125	4.102	0.020	1.327	0.023	0.066	--	bal
Filler wire	0.31	2.1	0.016	0.003	20.8	24.8	4.92	0.013	1.57	0.02	--	0.096	--

The received base metal was sliced in to coupons of dimensions of 150mmx75mmX5 mm thick sheets, using wirecut electrical discharge machining (WEDM) for carrying out the welding process. Standard V joint butt configurations (single V groove having a root gap of 1.2 mm, size and groove angle of 60°) were used for welding. Proper welding fixture with grooved copper backing strip was used to facilitate heat dissipation during welding. The fixture was clamped firmly to keep the base metals in proper alignment, so as to provide firm gripping and avoid distortion during the welding process. Joints prior to welding contact surfaces were cleaned with fresh stainless steel wire brush, followed by acetone swabbing.

The P-GMAW welding process parameters and their levels were established based on the preliminary welding trials and the parameters levels chosen for the current study are shown in Table 2. The welding was carried out based on the central composite rotatable design matrix and their coded and actual values are presented in Table 3.

**Table 2: Welding Process Parameters and their Levels**

Parameters	Symbol	-2	-1	0	1	2
Peak Current	$I_p$	340	350	360	370	380
Pulse Time	$t_p$	2.1	2.4	2.7	3	3.3
Pulse Frequency	$f$	120	125	130	135	140
Background Current	$I_b$	70	75	80	85	90
Welding Speed	$S$	30	35	40	45	50

Table 3: Coded and Actual Levels of the Five Variables

Exp. No.	I <sub>p</sub>	t <sub>p</sub>	f	I <sub>b</sub>	S	I <sub>p</sub> (Amps)	t <sub>p</sub> (Sec)	f (Hz)	I <sub>b</sub> (Amps)	S (mm/sec)
01	-1	-1	-1	-1	1	350	2.4	125	75	45
02	1	-1	-1	-1	-1	370	2.4	125	75	35
03	-1	1	-1	-1	-1	350	3	125	75	35
04	1	1	-1	-1	1	370	3	125	75	45
05	-1	-1	1	-1	-1	350	2.4	135	75	35
06	1	-1	1	-1	1	370	2.4	135	75	45
07	-1	1	1	-1	1	350	3	135	75	45
08	1	1	1	-1	-1	370	3	135	75	35
09	-1	-1	-1	1	-1	350	2.4	125	85	35
10	1	-1	-1	1	1	370	2.4	125	85	45
11	-1	1	-1	1	1	350	3	125	85	45
12	1	1	-1	1	-1	370	3	125	85	35
13	-1	-1	1	1	1	350	2.4	135	85	45
14	1	-1	1	1	-1	370	2.4	135	85	35
15	-1	1	1	1	-1	350	3	135	85	35
16	1	1	1	1	1	370	3	135	85	45
17	-2	0	0	0	0	340	2.7	130	80	40
18	2	0	0	0	0	380	2.7	130	80	40
19	0	-2	0	0	0	360	2.1	130	80	40
20	0	2	0	0	0	360	3.3	130	80	40
21	0	0	-2	0	0	360	2.7	120	80	40
22	0	0	2	0	0	360	2.7	140	80	40
23	0	0	0	-2	0	360	2.7	130	70	40
24	0	0	0	2	0	360	2.7	130	90	40
26	0	0	0	0	2	360	2.7	130	80	50
27	0	0	0	0	0	360	2.7	130	80	40
28	0	0	0	0	0	360	2.7	130	80	40
29	0	0	0	0	0	360	2.7	130	80	40
30	0	0	0	0	0	360	2.7	130	80	40
31	0	0	0	0	0	360	2.7	130	80	40
32	0	0	0	0	0	360	2.7	130	80	40



Figure 1: Photographic View of Welded Samples

Figure 1 is the Photographic views of P-GMAW joints. After welding, the weldments were subjected to non-destructive testing analysis to reveal the surface and subsurface defects. Further, these weldments were sliced in to specimens of different dimensions, according to ASTM standards using wire cut electrical discharge machining process to carry out various metallurgical and mechanical property tests for analysis.

**Metallurgical, Mechanical Characterization and Corrosion Resistance of the Weld Joints**

The macro/microstructure examinations were carried out on the cross sectional weld samples with the dimensions of 20 mm X 10 mm X 5 mm obtained from the weldments, keeping weld as center. Standard metallographic procedures were applied, including polishing with emery sheets of SiC of grit sizes varying from 200 to 1500, followed by disc polishing using diamond paste and aerosol on these samples to obtain a mirror finish on the weldments. Weld samples were etched with 10% oxalic acid, an electrolyte, to state and increase the contrast of the fusion zone with the base metal.

The tensile samples were prepared according to the AWS B 4.0 sub standards and tests were carried out at room temperature using Hounsfield Tensometer. In order to evaluate the Charpy impact toughness values of welded joints, a series of Charpy V-notch test was carried out on P-GMAW joints at room temperature. The specimens for Charpy test were taken perpendicular to weld direction according to the ASTM: E23. Notches were prepared exactly at the midpoint of the weld. Impact test was conducted for all welded samples and the value of the impact strength was recorded. The microhardness of weldment was measured in transverse direction using a Metco SMV 1000 micro Vickers hardness machine under 500 grams of load, maintained for dual time 15 seconds. The corrosion test was conducted as per ASTM G5 with the help of software based Ivium electrochemical system. The test specimens (working electrode) were polished to 2500 grit emery finish. A unit area of  $1 \text{ cm}^2$  was considered as the corrosion surface of the working electrode and all other areas were masked. The electrolyte of 3.5% NaCl was prepared by dissolving 35 g of NaCl in double distilled water. The pitting susceptibility of the weld joint was evaluated by using the 3.5%NaCl solution according to ASTM G48-03. The samples with a size of 20X10X5 mm, cut from the middle part of weld joint, were mechanically abraded with emery papers up to 2000 grit size step by step, mechanical polishing and subsequently cleaned with ethanol, and then, were tested in the water bath with a temperature of  $50 \pm 1^\circ\text{C}$  for 24 h. After the immersion test, the oxide film formed on the samples was removed by acid washing and the samples were subsequently cleaned with pure water. Pitting corrosion resistance of the weld regions in the weld joint was investigated by potentiodynamic polarization test in 3.5wt%NaCl solution at room temperature. The 10X10X 2 mm samples were embedded in epoxy resin leaving an exposed area of  $1 \text{ cm}^2$  used as working electrode surface. These working electrode surfaces were then mechanically ground to 2000 grit on SiC papers, followed by polished using a 2.5 mm diamond paste and then cleaned with pure water. The pure nitrogen gas ( $\text{N}_2$ ) was purged into the test solution for 30 min before the electrochemical test and continued to purge into the solution during the test. Before the test, the solution was stabilized at open circuit potential (OCP) for 30 min and potentiodynamic scan started from -200 mV versus OCP with a scan rate of 0.3333 mV/s until the current density increased to  $1 \text{ mA/cm}^2$ . At least three repeated potentiodynamic tests for each region were carried out to confirm the reproducibility. After the pitting tests, the pitting morphologies of the samples were observed by scanning electron microscope (JEOL Ltd., Tokyo, Japan).

## **RESULTS AND DISCUSSIONS**

### **Macrographs of the Joints**

The weld samples were sectioned to enable metallographic observations. The bead width and depth of penetrations were measured by optical microscopy, and some of the bead profiles are shown in Figure 2 (a-t).



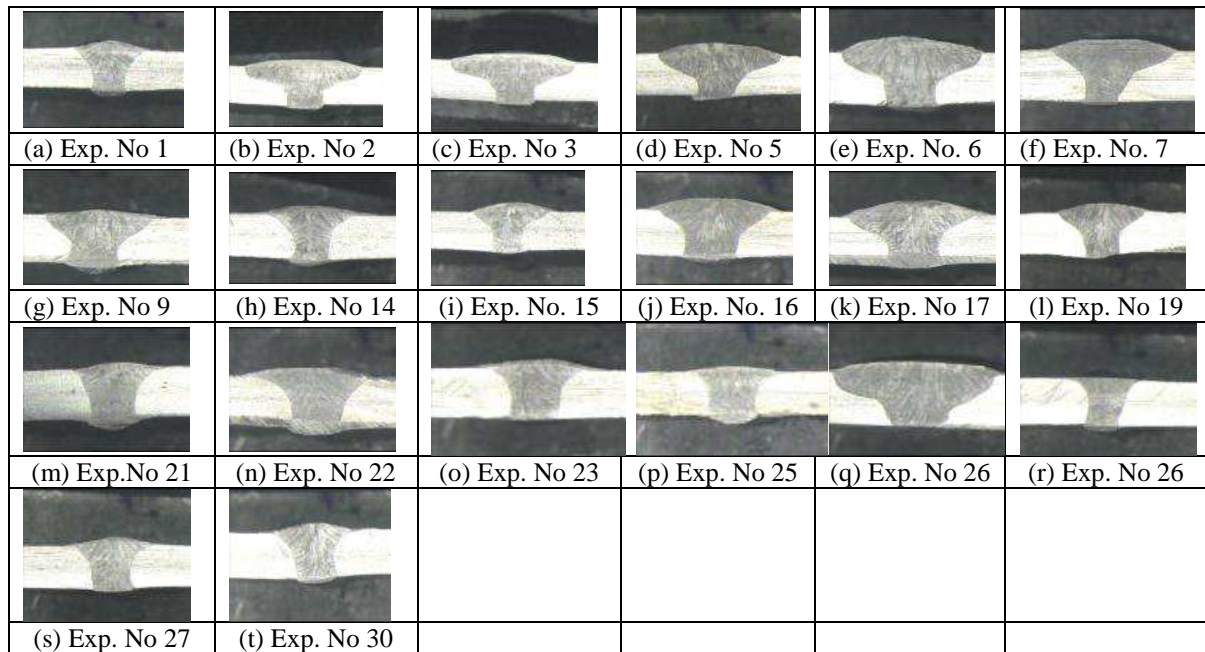


**Figure 2: (A-T). Typical Weld Bead Profiles of the Joints**

From the above bead profiles, no welding cracks or porosity are found in any of the welds as observed in bead profiles. All weld beads contain a full penetration.

#### Micro Structural Characterizations

The base material microstructure is presented in Figure 3. It exposed the well-defined grain boundaries. Typical microstructure near the weld junction of the pulsed gas metal arc weld joints is presented in Figure 4.

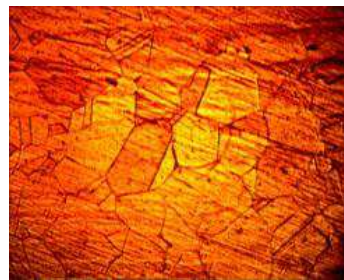


**Figure 3: Base Material Microstructure**

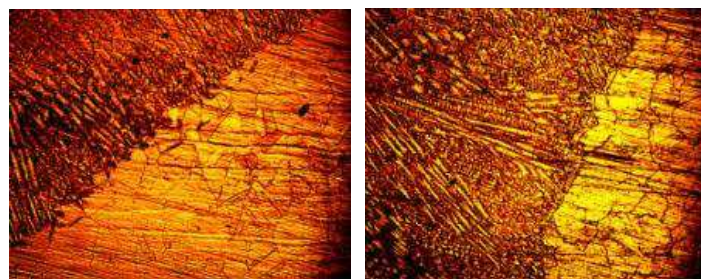


**Figure 4: Weld Junction Micrographs**

From Figure 4, the parent material and fusion zone could be discriminated easily and the heat affected zone remains negligible. The quantitative chemical compositions of the weld metals were confirmed by EDS investigations, and

their chemical composition of weld metals are presented in 3. The chromium and nickel equivalents ( $Cr_{eq}$  and  $Ni_{eq}$ ) with respect to the compositions of the P GMAW welded zone were determined using the following empirical relation [16]

$$Cr_{eq} = \% Cr + \% Mo + 0.7\% Nb; Ni_{eq} = \% Ni + 35\% C + 20\% N + 0.25\% Cu$$

**Table 4: Weld Metal Chemical Compositions & Ratio of  $Cr_{eq}/Ni_{eq}$**

Exp. No	Cr	Mo	Nb	Ni	C	N	Cu	$Cr_{eq}$	$Ni_{eq}$	$Cr_{eq}/Ni_{eq}$
1	19.82	4.91	0.02	23.51	0.014	0.07	1.39	24.74	25.74	0.961025
2	20.86	4.62	0.02	24.64	0.017	0.06	1.55	25.49	26.82	0.950471
3	20.24	4.74	0.03	24.65	0.014	0.08	1.54	25.00	27.12	0.921696
4	20.17	4.38	0.04	25.02	0.013	0.05	1.42	24.57	26.83	0.916064
5	19.87	4.89	0.05	24.88	0.012	0.07	1.58	24.79	27.09	0.915113
6	21.02	4.71	0.03	25.23	0.020	0.04	1.44	25.75	27.09	0.950572
7	20.10	4.85	0.04	24.97	0.018	0.08	1.56	24.97	27.59	0.905328
8	20.00	4.72	0.03	24.89	0.015	0.09	1.53	24.74	27.59	0.896494
9	20.74	4.56	0.04	24.94	0.018	0.07	1.49	25.32	27.34	0.926323
10	20.83	4.26	0.03	24.76	0.014	0.06	1.48	25.11	26.82	0.936279
11	19.98	4.63	0.04	24.95	0.015	0.09	1.52	24.63	27.65	0.890906
12	20.12	4.23	0.03	25.02	0.017	0.05	1.54	24.37	27	0.90263
13	19.93	4.54	0.03	24.90	0.015	0.09	1.49	24.49	27.59	0.887435
14	20.10	4.13	0.04	25.04	0.019	0.08	1.53	24.25	27.68	0.876135
15	19.99	4.71	0.04	25.03	0.014	0.07	1.49	24.72	27.29	0.906036
16	20.11	4.38	0.03	24.97	0.013	0.04	1.51	24.51	26.60	0.92138
17	19.78	4.27	0.04	24.56	0.017	0.06	1.49	24.07	26.72	0.90087
18	19.46	4.02	0.05	24.74	0.014	0.07	1.48	23.51	27	0.870926
19	20.16	4.51	0.04	24.15	0.013	0.09	1.44	24.69	26.76	0.922772
20	20.78	4.62	0.02	24.78	0.020	0.06	1.48	25.41	27.05	0.939519
21	20.61	4.71	0.03	24.84	0.019	0.08	1.46	25.34	27.47	0.922497
22	20.58	4.63	0.03	24.85	0.016	0.06	1.45	25.23	26.97	0.935434
23	20.72	4.71	0.04	24.73	0.013	0.07	1.46	25.45	26.95	0.944638
24	19.96	4.80	0.03	24.78	0.020	0.06	1.47	24.78	27.04	0.916203
25	19.84	4.79	0.03	24.63	0.018	0.09	1.44	24.65	27.42	0.899015
26	20.02	4.82	0.02	24.71	0.019	0.05	1.45	24.85	26.73	0.929556
27	19.46	4.12	0.02	24.56	0.020	0.08	1.49	23.59	27.23	0.866391
28	19.56	4.29	0.03	23.97	0.017	0.07	1.54	23.87	26.35	0.90592
29	20.34	4.36	0.04	24.06	0.016	0.08	1.51	24.72	26.59	0.929711
30,31,32	20.45	4.72	0.03	25.02	0.015	0.09	1.52	25.19	27.72	0.908602

The symbols denote the chemical compositions in weight percentage. The ratio of  $Cr_{eq}/Ni_{eq}$  for all weld metals is given in Table 4. From the weld metal chemical composition's (Table 3) point of view, it is clear that the alloys are in equilibrium and under high cooling rates they solidify as austenite mode. When the ratio of  $Cr_{eq}/Ni_{eq}$  is lower than 1.35, solidification results in austenitic formation and when it is greater than 1.35, ferrite formation has been reported (Lippold and Savage, (1979)). From Table 4, it is clearly understood that the ratio of  $Cr_{eq}/Ni_{eq}$  is lower than 1.35 i.e., with in the range of 0.866 (Exp. No.27) to 0.961 (Exp. No. 1) for all the weld metals. Hence, all the weld metals are solidified in austenitic solidification mode. Pseudo-binary diagram for the prediction of equilibrium microstructure in stainless steels is presented in Figure 5. Due to high cooling rates, all the weld metals are under equilibrium condition leading to the formation of austenite mode. The apparent presence of two phases has been detected and also attributed to the first

solidifying grains (dendrites) that are certainly enriched in austenite stabilizing elements, while the ferrite stabilizing elements are rejected in the interdendritic liquid [17]

The typical weld metal microstructures are presented in Figure 6 (a-p).

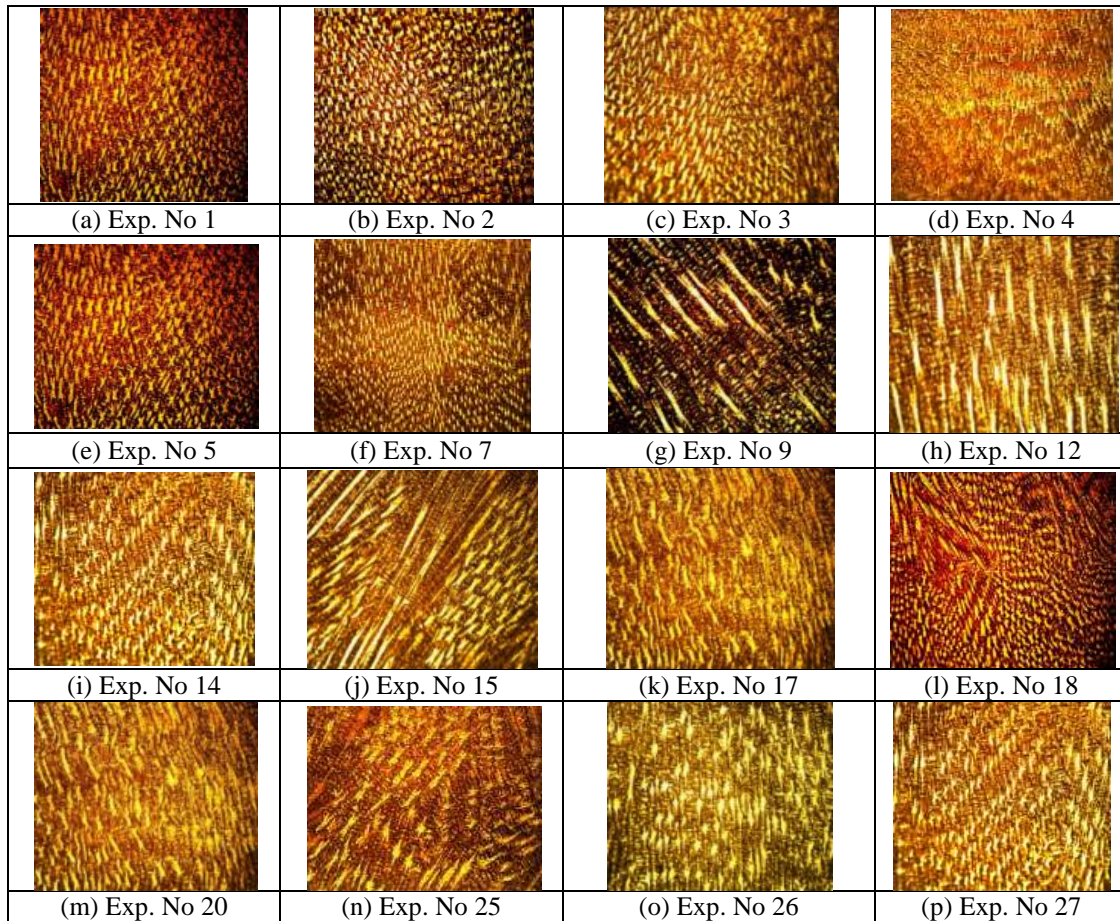


**Figure 6: (a-p) Typical Weld Metal Microstructures**

From Figure 6 (a-p), a full mixture of long columnar dendritic structures with equiaxed grains are observed and the dark phase that is visible in the primary dendritic phase and the lighter one is the secondary interdendritic phase. From Figure 6 (a-d), it is seen that the grains are finer with dendritic structures with equiaxed grains. A long columnar dendritic structure with elongated coarser grains is observed in Figure 6 (f, h, j, k, n and o). The austenitic stabilizing elements like Ni, N and C first get partitioned into the primary dendrites (darker phase-primary austenite phase). This leads to ferrite stabilizing elements like Cr, Mo and Si partitioning into the liquid phase. Along with the elements, partition of impurities is also formed into the liquid and becomes part of interdendritic (lighter one-Secondary phase) phase. From the weld metal chemical compositions (Table 4) it is clear that appreciable amount of nitrogen contents is present in all weld metals. When nitrogen present filler wire is used, the same gets dissolved in the weld pool and nitrogen content in the weld metal gets increased than the base material nitrogen content. Nitrogen is a more effective solid solution strengthening element than carbon and it also enhances grain refining. Nitrogen is a strong austenite stabilizer, thereby reducing the amount of nickel required for austenite stabilization and lowering the tendency to form ferrite. In gas tungsten arc welding of a super austenitic stainless steel with shielding gases and arc lengths yielding nitrogen contents in excess of 0.2%, more porosity is observed [18]. Even though the weld metal had high amount of nitrogen content, no porosity is observed



The percentage amounts of phases (dendritic & interdendritic) present in the weld metal were analysed by Metgi Inverter microscope loaded with DHS image data base (German make). After capturing the micrograph, it can launch the metallographic analysis from the convenient DHS image data base plug in interface. The original microstructure image colours were first converted to grey scale values. The area detection expansion module uses grey scale detection (phase analysis) to automatically calculate and process the area ratios by assigning a label and colour layer for phase identification. Then, numeric values were entered or the sliders were adjusted to define the upper and lower grey scale limits of each material phase. The measured percentages of phases, tensile strength, yield strength, % of elongation, impact toughness and corrosion resistance are presented in Table 5

**Table 5: Experimental Results  
(Tensile, Weld Metal Phase, Impact and Corrosion Resistance)**

Exp. No.	Tensile Strength (Mpa)	Yield Strength (Mpa)	% Elongation	Impact Toughness (J)	Weld metal phases (%)		Hardness
					Primary Dendritic Phase	Secondary Interdendritic Phase	
01	497	382	37	64	34	66	391
02	444	340	31	55	28	72	368
03	441	336	30	51	35	65	373
04	507	386	37	45	30	70	394
05	501	384	37	46	46	54	391
06	460	345	32	52	51	49	375
07	482	381	35	72	54	46	369
08	478	368	34	50	66	34	360
09	462	351	32	35	58	42	377
10	480	377	34	61	36	64	338
11	618	460	40	48	46	54	443
12	645	492	45	51	42	58	376
13	626	462	42	61	45	55	380
14	546	426	38	56	32	68	382
15	660	502	47	55	38	62	366
16	640	489	44	45	28	72	392
17	614	456	39	55	29	71	420
18	591	454	38	52	45	55	358
19	615	457	40	65	59	41	351
20	613	455	39	56	62	38	332
21	634	463	43	52	30	70	303
22	613	458	40	50	31	60	454
23	637	485	43	52	48	52	373
24	639	488	44	56	61	39	481
25	642	490	45	50	38	62	392
26	635	464	43	62	31	69	368
27	619	459	40	48	63	37	221
28	619	458	40	48	65	35	228
29	620	459	41	48	60	40	232
30	619	457	40	48	62	38	225
31	621	458	40	48	66	34	223
32	622	461	41	49	63	37	230

From Table 5, it is clearly seen that the percentage of secondary interdendritic phases present in the weld metal is much higher than the primary dendritic phases for all weld metals. Due to high amount of interdendritic, austenite can also be attributed to the high cooling rates, which makes the relevant coarsening of primary austenite dendrites difficult. In some of the weld metals (Table 5 - experiment No. 5, 8, 9, 11, 13, 18, 19 & 23), both the primary and secondary interdendritic phases were equally (approximately) present due to fast cooling rate.

### Tensile Strength of the Joints

The tensile samples were prepared according to the ASTM E 8 sub standards and the tests were performed at room temperature. The ultimate tensile strength, yield strength and percentage of elongation of all joints were evaluated. In each condition, three specimens were tested and the average tensile strength, yield strength and percentage of elongation of each specimen were obtained and are presented in Table 5. From Table 5, it is clear that majority of the weld metal tensile strength is much higher than the base metal tensile strength (570 Mpa) and few weld joint strengths are obtained from the 70%-80% of the base material strength. The tensile tested weld samples are presented in Figure 7. From Figure 7, it is clearly seen that in most of cases the fractures occur some distance away from the joint in the weld metal.



**Figure 7: Tensile Tested Weld Samples**

From the Table 5 (Exp. No 1-10), it is clear that the weld metal tensile strength is less when compared to the other weld joint strength and base metal tensile strength. During tensile tests, all the tensile samples underwent four typical stages including elastic deformation, plastic deformation, work hardening and fracture. The stages of plastic deformation and work hardening are more pronounced. This may be due to finer grain size present in the weld metal (Figure 6 (a-g)). Grain size and lower amount of primary dendrite phase present in the weld metal led to the reduction in the tensile properties of the joints. Experiment numbers 11-32 show that the weld metal tensile strength is much higher than the base metal strength. Due to higher percentage of secondary interdendritic phases present in the weld metal, the tensile strength of the joints is much higher. It is well accepted that the grain refinement is the key factor in improving the strength of welded samples [19]. The decrease of the grain size will dramatically increase the amount of grain boundaries, which further impedes dislocation motion, resulting in increase in the strength of the material. The traditional fine grain strengthening theory suggested that grain refinement can simultaneously improve the strength and ductility for most of materials. However, numerous literatures reported that grain refinement would decrease the ductility of high nitrogen steels and nitrogen containing austenitic stainless steel [20]. The fractured surface of tensile fractured specimen was analysed using SEM. The fracture surface of the tensile tested fractograph is shown in Figure 8.

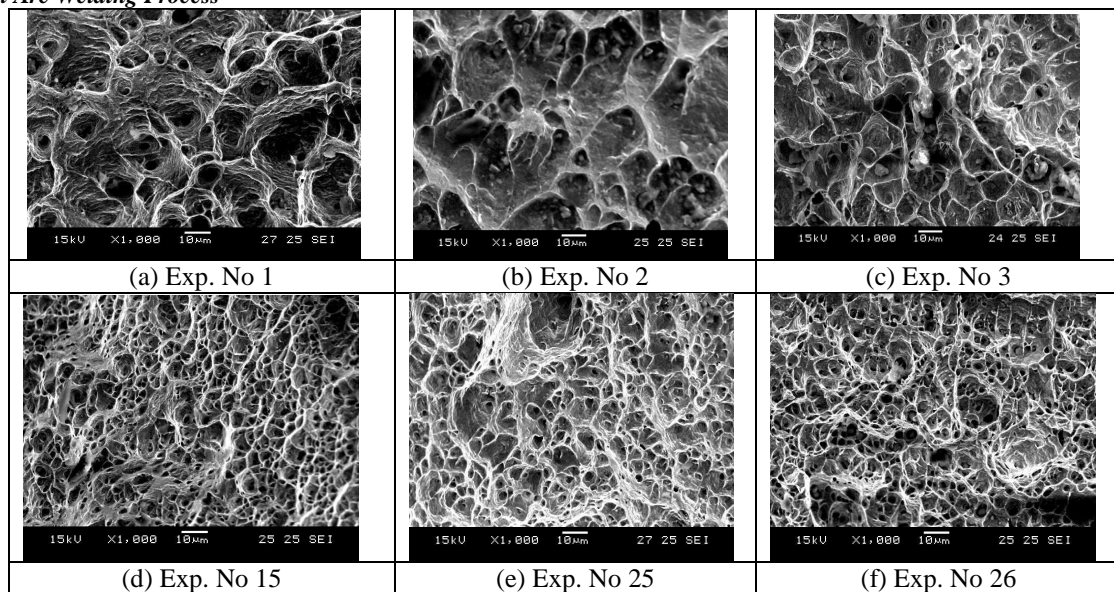


**Figure 8: (A-F) Typical SEM Fractrograph Microstructures of the Weld Joint**

The weld joints as revealed by the tensile fractographs (Figure 8 (a-c)) consist of coarser dimples and fine voids and some finer dimples are also seen distributed sparsely among coarser dimples. The size of the dimples can determine the strength of the weld joint. Because of coarser dimple size, the tensile strength of the joints are comparatively less. Figure 8 (d-f) reveals fine and uniform dimples, which indicate that the specimen fails in a ductile manner under the action of tensile loadingthere by a high tensile strength is obtained.

#### **Micro Hardness of the Weld Metal**

The microhardness (VHN) tests were performed on a transverse cross section of the weld metal parallel to the surface of the sheet in the centre of the welds using a load of 500 g, which was applied for the duration of 20 secs. The Microhardness values were measured moving from the base material across the weld bead towards its opposite side. According to the famous Hall-Petch formula [21], the obvious increment of hardness values in the weld metals can be attributed to high degree of grain refinement. During the solidification of the weld zone, the material generally loses its original strength induced by strain hardening. In the case of carbon and low alloy steels, the formation of bainite or martensitic phases in the weld zone promotes an increase of hardness. In single-phase materials, hardness increase in the weld zone is induced by precipitation hardening effects, residual stress, or microstructure refinement due to the rapid cooling of the weld pool. Due to refinement of the grain size, the weld metal hardness values are much higher than the base material hardness values. The microhardness profiles are presented in Figure 9 (a-c).

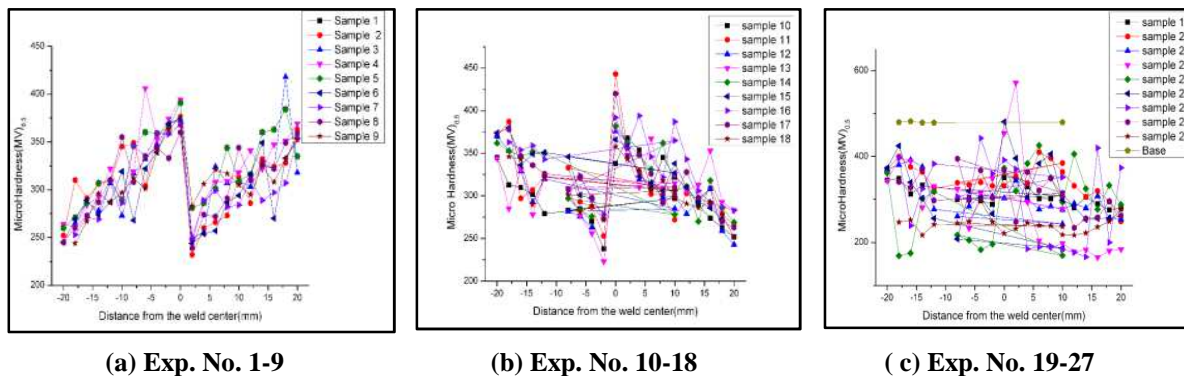


**Figure 9: (A-C) Micro Hardness of the Profiles**

As can be seen from Figure 9 (a-c), the hardness values increase moving from the base material across the weld joint towards its opposite side. This may be the result of the effect of rapid solidification. Rapid solidification increases under cooling and nucleation probability leads to very fine microstructure. At the same time it extends solute solubility which results in a supersaturated solid solution. From Figure 9 (a-c) it can be seen that increase in the hardness in the weld zone may be induced by precipitation hardening effects, residual stresses or microstructure refinement due to the rapid solidification of the weld pool. The columnar dendritic structure promotes the higher hardness than the equiaxed structure because of high dislocation density in the columnar structure. It is evident from the microstructure, majority of the phases were of long columnar dendritic structure with meeker amount of equiaxed structure that led to the increase in the hardness values in the weld metals

### Impact Toughness of the Weld Metals

The Charpy impact toughness values of all the joints were evaluated (room temperature) and the results are presented in Table 5. The photographic views of the prepared and tested impact test samples are presented in Figure 10 (a & b). The impact toughness of unwelded base metal is 60 Joules.

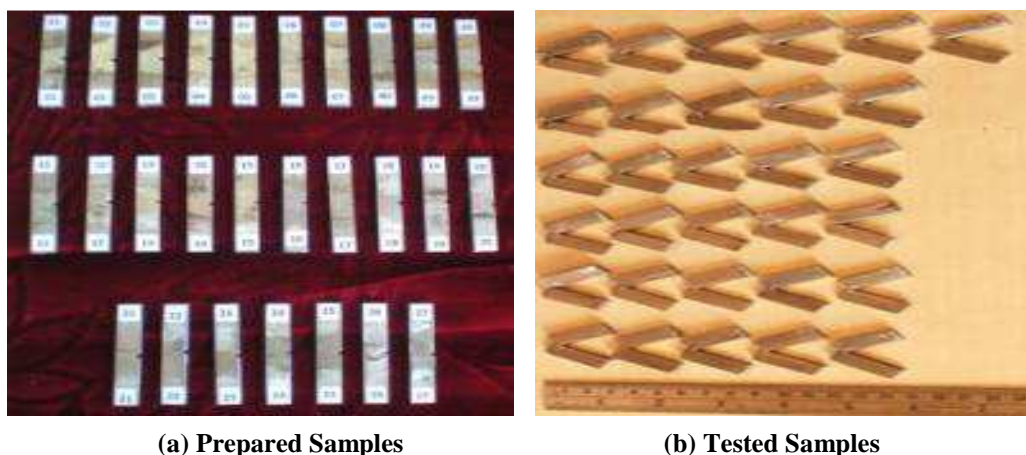


**Figure 10 (a & b) Charpy V notch samples**

From Table 5 it is clear that in experiment Nos 1, 7, 10, 13, the impact toughness values are higher than the base metal toughness. The improvement in toughness could be attributed to the refinement of grains at the weld metal. It shows that the energy absorption during impact testing of both the weldments was found to be better. In overall, all weld metal toughness values are in the range of 80% above the base metal toughness. In particular, in experiment number 9, toughness



value is very low compared to other welds, because of high amount of primary dendritic austenite phase present in the weld metal. The fractured surface of impact specimens were analyzed using SEM. The fractured surface of the impact tested fractograph is shown in Figure 11.

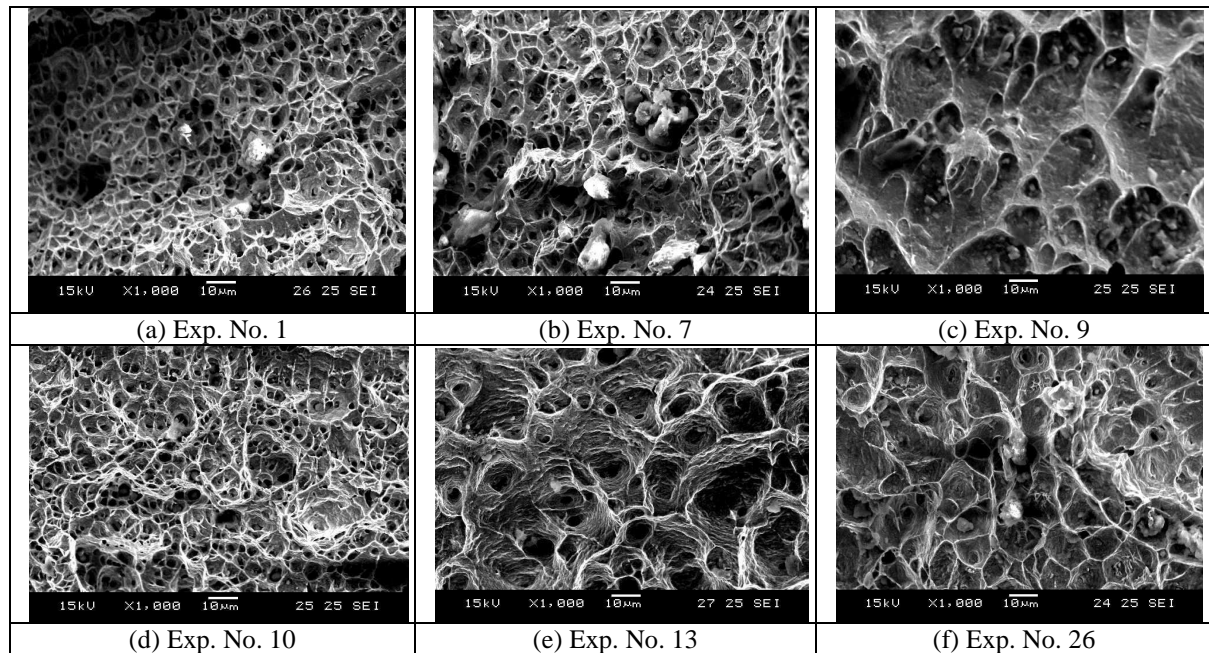


**Figure 11: (a-f) Typical SEM Fractograph Microstructures**

The impact specimen fracture surfaces of the all welded joints showed mixed mode fractures i.e., ductile and cleavage fractures. The dimple size exhibits a directly proportional relationship with strength and ductility, that is, if the dimple size is finer, then the strength and ductility of the respective joint is higher and vice versa. Figures 11 a, b, d, e & f show higher toughness values because of fine dimples, and Figure 11 (c) presents lower toughness values due to the presence of more elongated cavity shape. On the other hand, grain coarsening was observed in Experiment No 9 due to the slow cooling effects. Hence, the toughness of weld metal decreases due to grain coarsening.

#### **Pitting Corrosion Behaviour of the Weld Metal**

Apparently, weld metal which consisted of primary dendritic and secondary interdendritic austenite revealed that the preferential corrosion occurred in weld metal during pitting test. As indicated before, the rapid solidification and uncompleted phase transformation occurred during the welding process, and then the microsegregation existed in dendritic structure in weld metal, resulting in the formation of Cr-depleted zone in the dendrite boundaries. The experimentally obtained values of corrosion potential ( $E_{\text{corr}}$ ), corrosion current ( $I_{\text{corr}}$ ), polarization resistance (Ohm) and corrosion rate are listed in Table 5. Corrosion potential versus corrosion current density was plotted. Extrapolation of linear part to the corrosion potential gives the corrosion current. In anodic and cathodic plots, the slope of the linear part gives Tafel anodic and cathodic constants ( $B_a$  and  $B_c$ ) which are also present in the Table 5.

**Table 6 Results of Corrosion Potential ( $E_{\text{corr}}$ ), Corrosion Current ( $I_{\text{corr}}$ ) & corrosion rate**

Exp. No.	$I_{\text{corr}}$ (mA/cm <sup>2</sup> )	$E_{\text{corr}}$ (mV)	$B_a$ (mV)	$B_c$ (mV)	Polarization Resistance ( $\Omega$ )	Corrosion Rate (mm/year)
Base metal	0.0002304	-338.20	29.802	26.932	26696.87	0.005265
1	0.0002895	-365.93	36.458	70.262	24989.24	0.006615
2	0.0002874	-359.87	36.168	68.98	25843.69	0.006567
3	0.0002574	-336.15	30.523	39.445	26408.47	0.005882
4	0.0002468	-325.74	34.738	35.528	24621.57	0.005639
5	0.0002275	-300.64	29.683	33.791	22581.63	0.005198
6	0.0001234	-374.07	32.349	31.293	23042.98	0.00282
7	0.0001195	-310.83	31.391	30.421	30572.53	0.002731
8	0.0001012	-261.46	30.435	28.074	72077.63	0.002312
9	0.0001297	-266.18	36.094	41.045	61767.30	0.002964
10	0.0003824	-402.56	40.631	39.612	15472.39	0.008738
11	0.0003186	-398.93	38.298	36.347	20634.26	0.00728
12	0.0002101	-355.44	32.958	36.303	25748.74	0.004801
13	0.0002761	-355.62	72.148	65.762	25632.67	0.006309
14	0.0002673	-341.69	55.632	43.725	28732.84	0.006108
15	0.0002585	-331.83	40.174	35.631	30754.13	0.005907
16	0.0002370	-309.42	30.964	29.126	34793.16	0.005415
17	0.0002141	-324.87	31.284	32.164	32205.49	0.004892
18	0.0002145	-305.94	29.351	26.078	37990.14	0.004901
19	0.0003726	-400.48	41.378	40.531	20568.17	0.008514
20	0.0003799	-452.73	44.127	42.561	19692.83	0.008681
21	0.0003874	-461.54	45.264	43.267	18005.59	0.008852
22	0.0003911	-473.03	46.877	43.943	13312.64	0.008937
23	0.0004179	-483.72	47.823	44.276	13062.54	0.009549
24	0.0004297	-490.02	48.629	45.983	12808.31	0.009819
25	0.0004362	-388.73	47.998	44.732	23562.64	0.009967
26	0.0004417	-357.38	33.175	36.731	23045.74	0.010093
27	0.0001737	-335.76	32.482	35.092	23365.13	0.003969
28	0.0001727	-335.70	32.470	35.091	23106.56	0.003946
29	0.0001730	-335.72	32.481	35.090	22984.83	0.003953
30	0.0001736	-335.73	32.483	35.093	22856.16	0.003967
31	0.0001731	-335.74	32.478	35.091	22905.37	0.003955
32	0.0001734	-335.75	32.480	35.090	22910.83	0.003962

From Table 6, it is seen that experiment number 8 weld has a lower current density of 0.0001012 mA/cm<sup>2</sup> and a higher current density of 0.0004417 mA/cm<sup>2</sup>. Experiment No. 26 exhibits the best inhibitive characteristics. It also has the lowest corrosion rate and the highest polarization resistance, which show it to be the most effective concentration. Typical tafel curves for pulsed gas metal arc weld metals are shown in Figure 12 (a-l). Based on the corrosion rate values, experiment number 8, 7 and 6 welds showed the very best corrosion resistance due to high percentage of primary dendritic austenite phases present, and experiment number 26 and 25 welds have poor corrosion resistance due to higher percentage of secondary interdendritic austenite phases present in the weld metals.

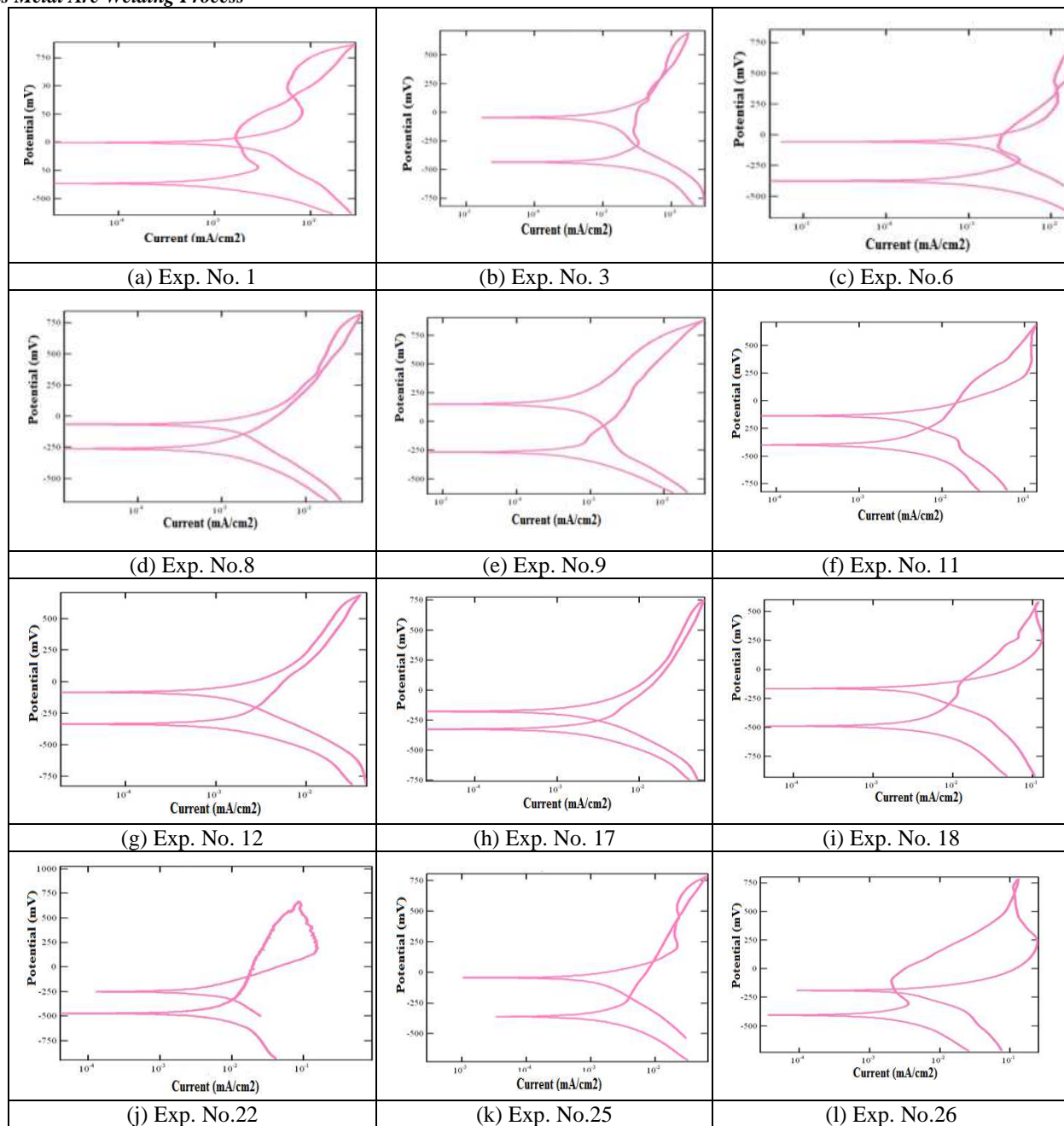


**Figure 12: (A-L) Cathodic and Anodic Polarization Tafel Curve of P GMAW Weld Metals**

Using Figure 12 (a-l), extrapolation methods were used and the  $I_{\text{corr}}$  and  $E_{\text{corr}}$  values were determined and are presented in Table 6. Pitting potential is defined as the potential at which current density began to increase continuously [22]. It is generally known that the local breakdown of a passive film followed by the occurrence of metastable pit and growth into a stable pit leads to abrupt increase in current density. However, it is interesting to see the fact that the current density increases moderately during the anodic polarization scan. This moderate increase in the current density suggests that this type of localized corrosion is more like selective corrosion than typical pitting corrosion [23]. The corroded surfaces were analyzed through the scanning electron microscopy (SEM) and SEM microstructures are presented in Figure 13 (a-f).



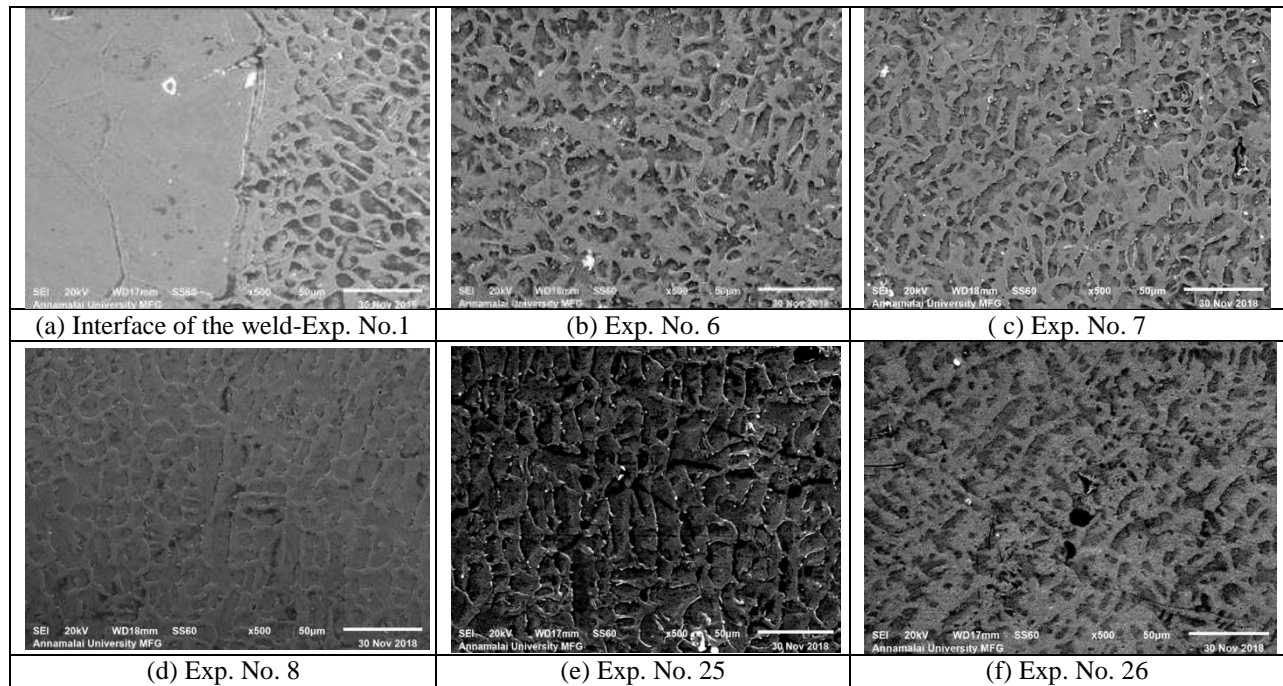


**Figure 13: (A-F) SEM Microstructure of the Corroded Surface**

Figure 13 (a-f) clearly indicates that the localized corrosion attacked along the grain boundary and also the secondary interdendritic phase region. The number of pits can be seen from the SEM micrographs (Figure 13 (b, c, e & f)). This justifies that the number of pits present in the weld area of PGMAW joint was lesser (Exp. No 6 7 & 8) than the others (Exp. No. 25 & 26). It also confirms that the corrosion resistance of the weld metal area is higher. In particular, in experiment no 8 weld metal area, the corrosion attacked area is very less i.e. pit formation is less. In experiment No 25 & 26 most of the pits are formed in grain boundary region. It confirms that the grain boundary is sensitive to pitting corrosion and due to this; the corrosion resistance is less compared to other welds. And also, primary dendritic phase is more prone to corrosion resistance, and hence the better pitting corrosion resistance is obtained in Exp. No. 8 than the other weld metals.

## CONCLUSIONS

In the present study, AISI 904 L super austenitic stainless steel sheet was successfully welded under different set of parameters by pulsed gas metal arc welding. The microstructure evolution, mechanical and corrosion properties of weldments were investigated. The main conclusions can be summarized as follows:

- Sound joints without any defects were acquired for all welds. From bead profiles, it was observed that all the welds had full penetration. Weld metal microstructure consists of a full mixture of long columnar dendritic structures with equiaxed grains. The weld metal contains fine grains. Microstructures exhibit primary dendrite and secondary interdendrite austenite phases. There is no ferrite and intermetallics.
- Most of the weld strength is higher than the base metal weld strength and a few weld strengths are 70-80% of the base metal strength. The weld joints as revealed by the tensile fractographs consist of coarser dimples and fine voids. The tensile specimens fail in a ductile mode under the action of tensile loading and a high tensile strength is obtained.



- Weld metal hardness increases due to precipitation hardening effects, residual stress, or microstructure refinement. Due to refinement of the grain size, the weld metal hardness values are much higher than the base material hardness values.
- In the experiment Nos 1, 7, 10 and 13, the impact toughness values are higher than the base metal toughness. In particular, in experimental number 9, toughness value is very low compared to other welds because of the presence of high amount of primary dendritic austenite phase in the weld metal. The impact specimen fracture surfaces of the all welded joints show mixed mode fractures, that is, ductile and cleavage fractures.
- In experiment numbers 8, 7 and 6, the welds have the very best corrosion resistance due to the presence of high percentage of primary dendritic austenite phases, and experiment number 26 and 25 welds have poor corrosion resistance due to the presence of higher percentage of secondary interdendritic austenite phases in the weld metals, which is also confirmed by SEM microstructures

## REFERENCES

1. Heino S, Knutson-Wedel M, Karlsson B. Precipitation behavior in heat affected zone of welded super austenitic stainless steel. *Mater SciTechnol* 1999;15: 101–8.
2. Heino S, Knutson-Wedel M, Karlsson B. Precipitation in a high nitrogen super austenitic stainless steel. *Mater SciTechnol Forum* 1999;318–320:143–8.
3. Svoboda M, Kroupa A, Soousek J, Vrestal J, Miodownik P. Phase changes in super austenitic steels after long-term annealing. *Zeitschrift Fur Metallkunde* 2004;95:1025–30.
4. Kumar, C. P., & Mohana, K. N. (2014). Corrosion inhibition efficiency and adsorption characteristics of some Schiff bases at mild steel/hydrochloric acid interface. *Journal of the Taiwan Institute of Chemical Engineers*, 45(3), 1031-1042.
5. Lee TH, Kim SJ, Jung YC. Crystallographic details of precipitates in Fe–22Cr–21Ni–6Mo–(N) super austenitic stainless steels aged at 900 °C. *Metal MaterTrans A* 2000;31:1713–23.
6. Simmons JW. Overview: high nitrogen alloying of stainless steels. *Mater SciEng A* 1996;207:159–69.
7. Molian PA (1985) Solidification behavior of laser welded stainless steel. *J Mater SciLett* 4:281–283.
8. DeepashriD, Nage RVS, Raman R (2006) Effect of nitrogen addition on the microstructure and mechanical behavior on 317 L and 904 L austenitic stainless steel welds. *J Mater Sci* 41:2097–2112
9. Bonollo F, Tiziani A, Tovo T, Volpone LM (2004) Super austenitic stainless steel: the microstructure and fatigue strength a welded joints. *Weld Int* 18(1):24–30
10. Ganesh, N., Kumar, M. U., Kumar, C. V., & Kumar, B. S. (2014). Optimization of cutting parameters in turning of EN 8 steel using response surface method and genetic algorithm. *International Journal of Mechanical Engineering and Robotics Research*, 3(2), 75.
11. Heino S, Knutson-wedel EM, Karlsson B (1999) Precipitation behaviour in heat affected zone of welded super austenitic stainless steel. *J Mater SciTechnol* 15(1):101–108.
12. P. Sathiya and M.Y. AbdulJaleel: Measurement of the bead profile and microstructural characterization of a CO2 laser welded AISI 904L super-austenitic stainless steel. *Opt. Laser Technol.* 42, 960–968 (2010).

13. S. Hertzman, R. JargeliusPettersson, R. Blom, E. Kivineva, and J. Eriksson: *Influence of shielding gas composition and welding parameters on the N-content and corrosion properties of welds in N- alloyed stainless steel grades. ISIJ Int.* 36(7), 968–976 (1996).
14. K. DevendranathRamkumar, AyushChoudhary, ShivangAggarwal, AnubhavSrivastava, TadikondaHarsha Mohan, and N. Arivazhagan, *Characterization of microstructure and mechanical properties of continuous and pulsed current gas tungsten arc welded super austenitic stainless steel*, Volume 30, Issue 10 28 May 2015 , pp. 1727-1746.
15. Singh, R. R., Gaikwad, A. B. H. I. S. H. E. K., Singh, S. S., & Singh, V. P. (2015). *Comparison of mechanical properties of medium carbon steel with dual phase steel. International Journal of Mechanical Engineering*, 4(4), 1-8.
16. K. Devendranath Ramkumar, Jelli Lakshmi Narasimha Varma, Gangineni Chaitanya, Ayush Choudhary, N.Arivazhagan, S.Narayanan, *Effect of autogeneous GTA welding with and without flux addition on the microstructure and mechanical properties of AISI904L joints*, *Materials Science & Engineering A*, 636(2015)1–9.
17. P.Sathiya, A. Sudhakaran and R.Soundararajan, *Mechanical and metallurgical investigation on gas metal arc welding of super austenitic stainless steel*, *International Journal of Mechanical and Materials Engineering (IJMME)*, Vol. 7 (2012), No. 1, 107–112.
18. T. KURSUN, *Effect of the GMAW and the GMAW-P welding processes on microstructure, hardness, tensile and impact strength of AISI 1030 steel joints fabricated by asp316l austenitic stainless steel filler metal*, *Archives of metallurgy and materials*, Volume 56, 2011, Issue 4, 955-963.
19. Molian, P.A. (1985) *Solidification behaviour of laser welded stainless steel. Journal of Materials science Letters*, 4, 281-283.
20. Rathod, C. H. A. N. D. A. R., & Reddy, G. K. (2016). *Experimental investigation of angular distortion and transverse shrinkage in CO2 arc welding process. International Journal of Mechanical Engineering*, 5(4), 21-28.
21. Raja, V.S., S.K. Varshney, R. Raman and S.D. Kulkarni (1998) *Influence of nitrogen on the pitting corrosion behavior of 904 L weld clad. Corrosion Science*, 40, 1609-1625.
22. StaffanHertzman, Rachel JargeliusPettersson, Roland Blom, EsaKivineva, and Jan Eriksson (1996) *Influence of shielding gas composition and welding parameters on the N-content and corrosion properties of welds in N-alloyed stainless steel grades. ISIJ International*, 36(7), 968-976.
23. H.B. Cui, G.M. Xie, Z.A. Luo, J. Ma, G.D.Wang, R.D.K.Misra, *Microstructural evolutionAnd mechanical properties of the stir zone in friction stir processed AISI201 stainless steel*, *Mater. Des.* 106 (2016) 463–475.
24. H.B. Li, Z.H. Jiang, H. Feng, S.C. Zhang, L. Li, P.D. Han, R.D.K. Misra, J.Z. Li, *Microstructure, mechanical and corrosion properties of friction stir welded high nitrogen nickel-free austenitic stainless steel*, *Mater. Des.* 84 (2015) 291–299.
25. S. Mironov, Y.S. Sato, H. Kokawa, H. Inoue, S. Tsuge, *Structural response of superaustenitic stainless steel to friction stir welding*, *Acta Mater.* 59 (2011)5472–5481.
26. H.Y. Ha, M.H. Jang, T.H. Lee, and J. Moon: *Understanding the relation between phase fraction and pitting corrosion resistance of UNS S32750 stainless steel. Mater.Charact.*106, 338 (2015).
27. M.H. Moayed and R.C. Newman: *Evolution of current transientsand morphology of metastable and stable pitting on stainless steelnear the critical pitting temperature. Corros.Sci.* 48, 1004 (2006).